



Source-Resolved Volatility and Oxidation State Decoupling in Wintertime Organic Aerosols in Seoul

Hwajin Kim^{1,2,*}, Jiwoo Jeong¹, Jihye Moon¹, Hyun Gu Kang^{2,3}

¹Department of Environmental Health Sciences, Graduate School of Public Health, Seoul National University, 08826 Seoul, South Korea

²Institute of Health and Environment, Graduate School of Public Health, Seoul National University, 08826 Seoul, South Korea

³Now at Multiphase Chemistry Department, Max Planck Institute for Chemistry, 55128 Mainz, Germany

Correspondence to: Hwajin Kim (khj0116@snu.ac.kr)

Abstract.

Organic aerosols (OA) are key components of wintertime urban haze, but the relationship between their oxidation state and volatility—critical for understanding aerosol evolution and improving model predictions—remains poorly constrained. While oxidation–volatility decoupling has been observed in laboratory studies, field-based evidence under real-world conditions is scarce, particularly during severe haze episodes. This study presents a field-based investigation of OA sources and their volatility characteristics in Seoul during a winter haze period, using a thermodenuder coupled with a high-resolution time-of-flight aerosol mass spectrometer (HR-ToF-AMS).

Positive matrix factorization resolved six OA factors: hydrocarbon-like OA, cooking, biomass burning, nitrogen-containing OA (NOA), less-oxidized oxygenated OA (LO-OOA), and more-oxidized OOA (MO-OOA). Despite having the highest oxygen-to-carbon ratio (~ 1.15), MO-OOA exhibited unexpectedly high volatility, indicating a decoupling between oxidation state and volatility. We attribute this to fragmentation-driven aging and autoxidation under stagnant conditions with limited OH exposure. In contrast, LO-OOA showed lower volatility and more typical oxidative behavior.

Additionally, NOA—a rarely resolved factor in wintertime field studies—was prominent during cold, humid, and stagnant conditions and exhibited chemical and volatility features similar to biomass burning OA, suggesting a shared combustion origin and meteorological sensitivity.

These findings provide one of the few field-based demonstrations of oxidation–volatility decoupling in ambient OA and highlight how source-specific properties and meteorology influence OA evolution. The results underscore the need to refine OA representation in chemical transport models, especially under haze conditions.

Keywords: Organic aerosol volatility, HR-ToF-AMS, Thermodenuder, elemental ratios, aging, fragmentation



31 1 Introduction

32 Atmospheric aerosols affect both human health and the environment by reducing visibility (Ghim et al., 2005; Zhao
33 et al., 2013) and contributing to cardiovascular and respiratory diseases (Hamanaka et al., 2018; Manisalidis et al.,
34 2020). In addition, aerosols play a significant role in climate change by scattering or absorbing solar radiation and
35 modifying cloud properties (IPCC AR6). Among the various aerosol components—including sulfate, nitrate,
36 ammonium, chloride, crustal materials, and water—organic aerosols (OA) are particularly important to characterize,
37 as they account for 20–90% of submicron particulate matter (Zhang et al., 2007). Identifying OA sources and
38 understanding their behavior are critical for effective air quality management; however, this is particularly
39 challenging due to the vast diversity and dynamic nature of OA compounds, which originate from both natural and
40 anthropogenic sources. Unlike inorganic aerosols, organic aerosols (OAs) evolve continuously through complex
41 atmospheric reactions, influenced by emission sources, meteorological conditions, and aerosol properties (Jimenez
42 et al., 2009; Hallquist et al., 2009; Robinson et al., 2007; Donahue et al., 2006; Ng et al., 2010; Cappa and Jimenez,
43 2010).

44 Volatility is a key parameter for characterizing organic aerosol (OA) properties, as it governs gas-to-particle
45 partitioning behavior and directly influences particle formation yields (Sinha et al., 2023). It also affects
46 atmospheric lifetimes and human exposure by determining how long aerosols remain suspended in the atmosphere
47 (Glasius and Goldstein, 2016). Therefore, accurately capturing OA volatility is essential for improving predictions
48 of OA concentrations and their environmental and health impacts. However, chemical transport models often
49 significantly underestimate OA mass compared to observations (Matsui et al., 2009; Jiang et al., 2012; Li et al.,
50 2017), largely due to incomplete precursor inventories and simplified treatment of processes affecting OA volatility.
51 For instance, aging—through oxidation reactions such as functionalization and fragmentation—can significantly
52 alter volatility by changing OA chemical structure (Robinson et al., 2007; Zhao et al., 2016). A recent study in
53 Korea further highlighted the importance of accounting for such processes when interpreting OA volatility under
54 ambient conditions (Kang et al., 2023). Given its central role in OA formation, reaction, and atmospheric
55 persistence, volatility analysis is critical for bridging the gap between measurements and model performance.

56 Traditionally, due to the complexity and variability of OA, the oxygen-to-carbon (O:C) ratio has been used as a
57 proxy for estimating volatility. In general, higher O:C values indicate greater oxidation and lower volatility
58 (Jimenez et al., 2009). Accordingly, many field studies classify oxygenated OA (OOA) into semi-volatile OOA
59 (SV-OOA) and low-volatility OOA (LV-OOA) based on their O:C ratios (Ng et al., 2010; Huang et al., 2010; Mohr



et al., 2012). However, this relationship is not always straightforward. Fragmentation during oxidation can increase both O:C and volatility simultaneously, disrupting the expected inverse correlation (Jimenez et al., 2009). In laboratory experiments, yields of highly oxidized SOA have been observed to decrease due to fragmentation (Xu et al., 2014; Grieshop et al., 2009). These findings suggest that while O:C can offer useful insights, it is insufficient alone to represent OA volatility. Direct volatility measurements, especially when paired with chemical composition data, are necessary to improve our understanding of OA sources and aging processes.

In this study, we investigate the sources and volatility characteristics of OA in Seoul during winter. Wintertime OA presents additional challenges due to its high complexity. During winter, emissions from combustion sources such as biomass burning and residential heating significantly increase, contributing large amounts of primary OA (Kim et al., 2017). Meanwhile, low ambient temperatures and reduced photochemical activity affect the formation and evolution of secondary OA (SOA). Frequent haze events further complicate the aerosol properties by extending aging times and increasing particle loadings. These overlapping sources and atmospheric conditions make winter OA particularly difficult to characterize and predict. Seoul, however, comprehensive studies on OA volatility during winter remain limited, despite the season's significance for air quality management. To address these goals, we conducted real-time, high-resolution measurements using a high-resolution time-of-flight aerosol mass spectrometer (HR-ToF-AMS) coupled with a thermodenuder (TD). The objectives of this study are to: (1) improve the understanding of wintertime OA in Seoul, (2) characterize the volatility of OA associated with different sources, and (3) explore the relationship between OA volatility and chemical composition.

2 Experimental methods

2.1 Sampling Site and Measurement Period

Continuous real-time measurements were conducted in Seoul, the capital of South Korea, where a previous study (Kim et al., 2017) was also performed. Detailed descriptions of the measurement site can be found in that reference. Briefly, the sampling site was located in the northeastern part of the city (37.60° N, 127.05° E), approximately 7 km from the city center. Air samples were collected at an elevation of approximately 60 meters above sea level, on the fifth floor of a building. The site is situated near major expressways and is surrounded primarily by commercial and residential areas, indicating substantial influence from anthropogenic and primary emission sources (Kim et al., 2017). Measurements were carried out from November 28 to December 28, 2019. During this period, the



87 average ambient temperature was 1.76 ± 4.3 °C, and the average relative humidity (RH) was $56.9 \pm 17.5\%$, based
88 on data from the Korea Meteorological Administration (<http://www.kma.go.kr>).

89 **2.2 Instrumentation and Measurements**

90 The physico-chemical properties of non-refractory PM₁ (NR-PM₁) species—including sulfate, nitrate, ammonium,
91 chloride, and organics—were measured using an Aerodyne high-resolution time-of-flight aerosol mass
92 spectrometer (HR-ToF-AMS) (DeCarlo et al., 2006). Data were acquired at 2.5-minute intervals, alternating
93 between V and W modes. The V mode provides higher sensitivity but lower resolution, suitable for mass
94 quantification, whereas the W mode offers higher mass resolution but lower sensitivity, used here for OA source
95 apportionment. Simultaneously, black carbon (BC) concentrations were measured at 1-minute intervals using a
96 multi-angle absorption photometer (MAAP; Thermo Fisher Scientific, Waltham, MA, USA). Total PM₁ mass was
97 calculated as the sum of NR-PM₁ and BC.

98 Hourly trace gas concentrations (CO, O₃, NO₂, SO₂) were obtained from the Gireum air quality monitoring station
99 (37.61° N, 127.03° E), managed by the Seoul Research Institute of Public Health and Environment. Meteorological
100 data (temperature, RH, wind speed/direction) were collected from the nearby Jungreung site (37.61° N, 127.00°
101 E). All data are reported in Korea Standard Time (UTC+9).

102 To examine aerosol volatility, a thermodenuder (TD; Envalytix LLC) was installed upstream of the HR-ToF-AMS.
103 Details are provided in Supplementary Section S1 Kang et al. (2022). Briefly, ambient flow alternated every 5
104 minutes between a TD line and a bypass line at 1.1 L min⁻¹. Residence time in the TD line was ~6.3 s. The TD
105 setup included a 50 cm heating section followed by an adsorption unit. Heated particles were stripped of volatile
106 species, while the downstream carbon-packed section prevented recondensation. TD temperature cycled through
107 12 steps (30 to 200 °C), with each step lasting 10 min (total cycle = 120 min). AMS V and W modes were alternated
108 during the same cycle. The heater was pre-adjusted to the next temperature while the bypass was active.

109

110 **2.3 Data Analysis**

111

112 **2.3.1 Data analysis and OA Source Apportionment**

113 HR-AMS data were processed using SQUIRREL v1.65B and PIKA v1.25B. Mass concentrations of non-refractory
114 PM₁ (NR-PM₁) species were derived from V-mode data, while high-resolution mass spectra (HRMS) and the



115 elemental composition of organic aerosols (OA) were obtained from W-mode data. Elemental ratios (O:C, H:C,
116 and OM/OC) were calculated using the Improved-Ambient (IA) method (Canagaratna et al., 2015). Positive Matrix
117 Factorization (PMF) was applied to the HRMS of organics using the PMF2 algorithm (v4.2, robust mode) (Paatero
118 and Tapper, 1994). The HRMS and corresponding error matrices from PIKA were analyzed using the PMF
119 Evaluation Tool v2.05 (Ulbrich et al., 2009). Data pretreatment followed established protocols (Ulbrich et al., 2009;
120 Zhang et al., 2011).

121 A six-factor solution ($f_{\text{Peak}} = 0$; $Q/Q_{\text{expected}} = 3.56$) was selected as optimal (Fig. S1). The resolved OA sources
122 included hydrocarbon-like OA (HOA; 14%; O:C = 0.13), cooking-related OA (COA; 21%; O:C = 0.18), nitrogen-
123 enriched OA (NOA; 2%; O:C = 0.22), biomass-burning OA (BBOA; 13%; O:C = 0.25), less-oxidized oxygenated
124 OA (LO-OOA; 30%; O:C = 0.68), and more-oxidized oxygenated OA (MO-OOA; 20%; O:C = 1.15) (Figs. S2 and
125 S3). Alternative five- and seven-factor solutions were also evaluated. In the five-factor solution, the biomass
126 burning source was not clearly resolved and appeared to be distributed across multiple factors. In the seven-factor
127 solution, BBOA was further split into two separate factors without clear distinction or added interpretive value,
128 making the six-factor solution the most physically meaningful and interpretable (Figs. S4 and S5).

129

130 2.3.2 Thermogram and Volatility Estimation

131 The chemical composition dependent mass fraction remaining (MFR) was derived at each TD temperature by
132 dividing the corrected mass concentration of the TD line [p] by the average of the adjacent bypass lines [p-1] and
133 [p+1]. Thermograms were corrected for particle loss, estimated using reference substances like NaCl, which exhibit
134 minimal evaporation (Huffman et al., 2009; Saha et al., 2014; Kang et al., 2023). OA factor concentrations at each
135 TD temperature were derived via multivariate linear regression between post-TD HRMS and ambient OA factor
136 HRMS profiles as described in Zhou et al., 2016.

137 Volatility distributions were modeled using the thermodenuder mass transfer model from Riipinen et al. (2010) and
138 Karnezi et al. (2014), implemented in Igor Pro 9 (Kang et al., 2022). OA mass was distributed into eight logarithmic
139 saturation concentration bins (C^* : 1000 to $0.0001 \mu\text{g m}^{-3}$). Modeled MFRs were fit to observations using Igor's
140 "FuncFit" function, repeated 1,000 times per OA factor to determine best-fit results. The model assumes no thermal
141 decomposition and includes adjustable parameters: mass accommodation coefficient (α_m) and enthalpy of
142 vaporization (ΔH_{exp}), randomly sampled within literature-based ranges (Table S1).

143

144 3 Results and discussion



145 3.1 Overview of PM₁ Composition and OA Sources

146 The time series of submicron aerosol (PM₁ = NR-PM₁ + BC) mass concentrations measured by the AMS (non-
147 refractory species) and MAAP (black carbon) are shown in Fig. S6, along with gaseous pollutants such as CO, SO₂,
148 and O_x (O_x = O₃ + NO₂), and meteorological parameters including relative humidity (RH), temperature, wind
149 direction, and wind speed. The mean PM₁ concentration during the study period was moderate, at $27.8 \pm 15.3 \mu\text{g}$
150 m^{-3} .

151 Organics (41%) and nitrate (30%) were the most abundant chemical components of PM₁, followed by ammonium
152 (12%), sulfate (10%), BC (5%), and chloride (3%) (Fig. 1a). Among the organic aerosols, six OA factors were
153 identified during the winter of 2019: hydrocarbon-like OA (HOA; 14%; O:C = 0.13), cooking-related OA (COA;
154 21%; O:C = 0.18), nitrogen-enriched OA (NOA; 2%; O:C = 0.22), biomass burning OA (BBOA; 13%; O:C =
155 0.25), and two types of secondary organic aerosols—less-oxidized oxygenated OA (LO-OOA; 30%; O:C = 0.68)
156 and more-oxidized oxygenated OA (MO-OOA; 20%; O:C = 1.15) (Fig. 1e and Fig. S2). These compositions are
157 consistent with previous wintertime observations in Kim et al. (2017), with the exception of NOA, which will be
158 discussed in detail in Section 3.1.1.

159 PM₁ mass concentrations varied widely, ranging from 4.61 to 91.4 $\mu\text{g m}^{-3}$, largely due to two severe haze episodes
160 that occurred between December 7–12 and December 22–26 (Fig. 1). During these episodes, average
161 concentrations increased significantly, driven primarily by elevated levels of nitrate, MO-OOA, and NOA (Fig.
162 1f,g). These results suggest that the haze events were caused by local accumulation of emissions and enhanced
163 SOA formation under stagnant meteorological conditions. Such haze episodes, characterized by local emission
164 buildup and secondary aerosol production, are a typical wintertime feature, as also reported in Kim et al. (2017).

165 3.1.1 Nitrogen-containing organic aerosol (NOA)

166 Unlike previous wintertime aerosol studies in Seoul, this study successfully resolved a nitrogen-containing organic
167 aerosol (NOA) factor by applying positive matrix factorization (PMF) to high-resolution AMS data. NOA
168 contributed approximately 2% of the total organic aerosol (OA) mass—comparable to urban observations in
169 Guangzhou (3%; Chen et al., 2021), Pasadena (5%; Hayes et al., 2013), and New York (5.8%; Sun et al., 2011).

170 Detection of particulate NOA using real time measurement has been challenging due to its low concentration and
171 high volatility. Although Baek et al. (2022) identified nitrogen-containing species in Seoul via year-round filter-
172 based molecular analysis, PMF-based resolution of NOA in real time has not been previously reported. The



173 successful identification in this study is likely attributable to favorable winter meteorological conditions—
174 specifically low temperatures (-0.24°C) and persistently high relative humidity ($\sim 57\%$) compared to the 2017
175 winter season (Kim et al., 2017)—that enhanced gas-to-particle partitioning of semi-volatile amines, thereby
176 enabling their detection (Fig. S2). NOA concentrations frequently exceeded $1\text{ }\mu\text{g m}^{-3}$ when RH surpassed 60% (Fig.
177 2), supporting the importance of RH-driven partitioning and the subsequent formation of low-volatility aminium
178 salts (Milic et al., 2016). Although extremely low temperatures may inhibit NOA formation due to the transition
179 of aerosol particles into solid phase (Ge et al., 2011; Srivastava et al., 2022), the combination of consistently cold
180 and humid conditions during the measurement period likely promoted the partitioning of semi-volatile amines into
181 the particle phase.

182 In addition, episodic haze events further elevated NOA levels, increasing its contribution to OA from 1% during
183 clean periods to as much as 3% (Fig. 1f–h). These high-concentration events likely improved the signal-to-noise
184 ratio, facilitating PMF resolution. Back-trajectory analysis linked these events to regional recirculation patterns
185 (Cluster 1, Fig. S7), suggesting a predominantly local origin—consistent with the short atmospheric lifetimes and
186 high reactivity of most amines.

187 The NOA factor exhibited the highest nitrogen-to-carbon (N:C) ratio (0.22) and the lowest oxygen-to-carbon (O:C)
188 ratio (0.19) among all POA factors (Fig. S2), indicating a chemically reduced, nitrogen-rich composition. Its mass
189 spectrum was dominated by amine-related fragments including m/z 30 (CH_4N^+), 44 ($\text{C}_2\text{H}_6\text{N}^+$), 58, and 86 (Fig. 3a),
190 closely matching reference spectra of low-molecular-weight alkylamines such as dimethylamine (DMA),
191 trimethylamine (TMA), methylamine (MA), and dibutylamine (DBA) (Fig. 3b–e). These amines are commonly
192 emitted during the combustion of nitrogen-rich biomass and proteinaceous materials and are frequently associated
193 with biomass burning emissions (Ge et al., 2011). While other amines like triethylamine (TEA), diethylamine
194 (DEA), and ethylamine (EA) may contribute, their typical sources—such as industrial processes, solvent use, or
195 wastewater treatment (E. Poste et al., 2014; He et al., 2016; Ge et al., 2011)—are distinct from biomass combustion,
196 and thus they are considered less likely to be the dominant contributors under wintertime conditions in Seoul.
197 Previous molecular analysis by Baek et al. (2022) also supports DMA, MA, and TMA as the main amine species
198 observed during December in Seoul.

199 Supporting this, NOA exhibited a diurnal pattern similar to that of BBOA, with both peaking at night and in the early morning
200 (Fig. 2a), suggesting shared sources or formation mechanisms. Biomass burning under cold, oxygen-limited conditions is
201 known to emit various amines and amides (You et al., 2014; Yao et al., 2016), which may contribute directly to NOA or serve



202 as precursors for its secondary formation. Strong correlations with CH_4N^+ ($r = 0.95$) and $\text{C}_2\text{H}_6\text{N}^+$ ($r = 0.91$) (Fig. 2) further
203 support the presence of reduced nitrogen compounds, typically associated with residential fuel combustion and wintertime
204 heating. However, the time series of NOA and BBOA were not well correlated (Fig. 2 and S7), likely because NOA episodes
205 preferentially occurred during haze periods under stagnant conditions (Fig. 1), whereas BBOA emissions tend to follow a more
206 regular, daily emission pattern. Under cold, humid, and stagnant conditions, these semi-volatile amines can readily partition
207 into the particle phase and form low-volatility aminium salts, enhancing the observed NOA signal. Taken together, these
208 results suggest that NOA during wintertime in Seoul is strongly influenced by a combination of combustion-related
209 primary emissions and subsequent atmospheric processing of amine-containing species, facilitated by seasonally
210 favorable conditions.

211 3.1.2 Secondary organic aerosols (SOA)

212 In this study, two oxygenated organic aerosol (OOA) factors—more-oxidized OOA (MO-OOA) and less-oxidized
213 OOA (LO-OOA)—were identified, together accounting for approximately half of the total organic aerosol (OA)
214 mass. This fraction is notably higher than that reported in previous wintertime urban studies (Kim et al., 2017;
215 Zhang et al., 2007). Both OOAs exhibited characteristic mass spectral features, including prominent peaks at m/z
216 44 (CO_2^+) and m/z 43 ($\text{C}_2\text{H}_3\text{O}^+$), which are widely recognized as markers of oxygenated organics (Fig. S2e, S3f).
217 The oxygen-to-carbon (O:C) ratios for MO-OOA and LO-OOA were 1.15 and 0.68, respectively, indicating highly
218 oxidized chemical compositions. The O:C ratio of MO-OOA was especially elevated, exceeding those reported in
219 previous Seoul campaigns—0.68 in winter 2015 (Kim et al., 2017), 0.99 in spring 2019 (Kim et al., 2020), and
220 0.78 in fall 2019 (Jeon et al., 2023)—while the LO-OOA ratio was within a similar range.

221 MO-OOA showed strong correlations with secondary inorganic species such as nitrate ($r = 0.90$), ammonium ($r =$
222 0.92), and sulfate ($r = 0.81$), consistent with its formation through regional and local photochemical aging processes
223 (Fig. S3). In contrast, LO-OOA exhibited only moderate correlations with these inorganics ($r = 0.50, 0.51$, and 0.42 ,
224 respectively), which may suggest an additional influence from other semi-primary sources not strongly associated
225 with inorganic secondary species such as biomass burning. This interpretation is further supported by a minor signal
226 at m/z 60—indicative of levoglucosan, a known tracer for biomass burning (Fig. S2). The weaker coupling with



secondary inorganics implies that LO-OOA may represent a mixture of aged and semi-primary organics, partially derived from combustion-related activities.

3.1.3 Primary organic aerosols (POA)

Three primary organic aerosol (POA) factors were identified in this study: hydrocarbon-like OA (HOA), cooking-related OA (COA), and biomass burning OA (BBOA). These three components exhibited mass spectral and temporal characteristics consistent with previous observations in Seoul and other urban environments. HOA was characterized by dominant alkyl fragment ions ($C_nH_{2n+1}^+$ and $C_nH_{2n-1}^+$; Fig. S2a) and a low O:C ratio (0.13), consistent with traffic-related emissions (0.05–0.25) (Canagaratna et al., 2015). It showed strong correlations with vehicle-related ions $C_3H_7^+$ ($r = 0.79$) and $C_4H_9^+$ ($r = 0.86$) (Kim et al., 2017; Canagaratna et al., 2004; Zhang et al., 2005), and exhibited a distinct morning rush hour peak (06:00–08:00), followed by a decrease likely driven by boundary layer expansion (Fig. S3a).

COA, accounting for 21% of OA, showed higher contributions from oxygenated ions than HOA, with tracer peaks at m/z 55, 84 and 98 (Fig. S2b) consistent with cooking emissions (Sun et al., 2011). It correlated strongly with cooking-related ions such as $C_3H_3O^+$ ($r = 0.94$), $C_5H_8O^+$ ($r = 0.96$), and $C_6H_{10}O^+$ ($r = 0.98$) (Fig. S3h), and displayed prominent peaks during lunch and dinner hours, reflecting typical cooking activity patterns.

BBOA was identified based on characteristic ions at m/z 60 ($C_2H_4O_2^+$) and 73 ($C_3H_5O^+$), both of which are associated with levoglucosan—a well-established tracer for biomass burning (Simoneit et al., 2002). Its relatively high f_{60} and low f_{44} values (Fig. S8a) indicate that the BBOA observed in this study was relatively fresh and had not undergone extensive atmospheric aging (Cubison et al., 2011). Furthermore, BBOA exhibited moderate correlations with NOA in both diurnal profiles and time series (Fig. 2), particularly with nitrogen-containing ions such as $C_2H_4N^+$ ($r = 0.67$) and $C_2H_6N^+$ ($r = 0.56$) (Fig. 2 and S3), which are also dominant peaks in the NOA mass spectrum. This overlap suggests a potential shared emission source or co-emission scenario, such as biomass burning, which is known to emit both organic aerosols and reduced nitrogen-containing compounds.

3.2 Volatility of Non-Refractory Species

Figure 4 presents thermograms of non-refractory (NR) species measured by HR-ToF-AMS. The mass fraction remaining (MFR) after thermodenuder (TD) treatment follows the typical volatility trend reported in previous studies (Xu et al., 2016; Kang et al., 2022; Jeon et al., 2023; Huffman et al., 2009): nitrate was the most volatile,



254 followed by chloride, ammonium, organics, and sulfate. Nitrate showed the steepest decline with temperature, with
255 a T_{50} of $\sim 67^\circ\text{C}$ —higher than pure ammonium nitrate ($\sim 37^\circ\text{C}$; Huffman et al., 2009), suggesting contributions from
256 less volatile species like organonitrates or metal nitrates (Feng et al., 2023). Nearly complete evaporation occurred
257 by 200°C ($\sim 2\%$ remaining). Compared to fall ($T_{50} \sim 73^\circ\text{C}$, incomplete evaporation), winter nitrate appeared more
258 volatile, supporting enhanced NOA detection and indicating relatively fewer non-volatile nitrate forms. Sulfate was
259 the least volatile ($T_{50} \sim 170^\circ\text{C}$), consistent with ammonium sulfate (Scott and Cattell, 1979). A subtle slope change
260 near 140°C may suggest phase transitions or less volatile sulfate components. About 25% remained at 200°C ,
261 indicating possible contributions from metallic or organic sulfates. Ammonium showed intermediate volatility,
262 with T_{50} between nitrate and sulfate. Its slightly lower winter T_{50} suggests stronger nitrate association. Residual
263 ammonium at 200°C was consistent ($\sim 4\%$) across seasons (Kang et al., 2022; Jeon et al., 2023). Chloride volatility
264 was also comparable between seasons in terms of T_{50} , but exhibited more complete evaporation in winter ($\sim 4\%$
265 residual vs. $\sim 10\%$ in fall), possibly reflecting a shift in source to more volatile forms like road salt during
266 wintertime.

267 Organic aerosol (OA) exhibited moderate volatility ($T_{50} \sim 120^\circ\text{C}$), consistent with the presence of a wide variety
268 of compounds with differing volatilities. This trend aligns with spring and fall observations (Kang et al., 2022; Jeon
269 et al., 2023).

270 3.2.1 Volatility Profiles of Organic sources

271 Figure 5 presents the volatility distributions of six OA sources within the volatility basis set (VBS) framework.
272 Volatility is expressed as the effective saturation concentration (C^* , $\mu\text{g m}^{-3}$), where higher C^* values correspond
273 to higher volatility. Following Donahue et al. (2009), C^* values are categorized into four bins: extremely low-
274 volatility organic compounds (ELVOCs, $\log C^* < -4.5$), low-volatility organic compounds (LVOCs, $-4.5 < \log$
275 $C^* < -0.5$), semi-volatile organic compounds (SVOCs, $-0.5 < \log C^* < 2.5$), and intermediate-volatility organic
276 compounds (IVOCs, $2.5 < \log C^* < 6.5$).

277 Among the primary OA (POA) sources, hydrocarbon-like OA (HOA) exhibited the highest volatility, with mass
278 predominantly distributed in the SVOC and IVOC ranges. This is consistent with its low oxidation state ($\text{O:C} =$
279 0.35) and primary emission characteristics. Mass fraction remaining (MFR) results (Fig. S9) further support this,
280 showing rapid mass loss at lower temperatures. Biomass burning OA (BBOA) and nitrogen-containing OA (NOA)
281 also showed high volatility, peaking in the SVOC–IVOC range ($\log C^* = 1\text{--}3$), and had lower O:C ratios of 0.25



282 and 0.19, respectively. Their slightly more oxidized nature relative to HOA, despite a similar volatility range, may
283 reflect emissions occurring under nighttime or cooler conditions, which promote condensation of otherwise volatile
284 species. The similar volatility distributions and MFR profiles of BBOA and NOA (Fig. S9) further support the
285 possibility of a shared emission source or formation pathway (Section 3.1.1). Cooking-related OA (COA) showed
286 a more moderate volatility profile, with mass more evenly distributed across the LVOC and SVOC bins. This
287 pattern reflects its diverse cooking sources and variable emission profiles (Kang et al., 2022).

288 For secondary OA (SOA), less-oxidized oxygenated OA (LO-OOA) exhibited the lowest volatility, with substantial
289 mass in the LVOC and ELVOC bins ($C^* \approx 10^{-3}$ – 10^{-4}), consistent with its aged, highly condensed nature. This is in
290 agreement with previous findings in Seoul during spring (Kang et al., 2022). In contrast, more-oxidized OOA (MO-
291 OOA), despite its higher oxidation state ($O:C = 1.15$), displayed greater volatility, with a peak at $C^* \approx 10^1$. This
292 discrepancy likely reflects differences in formation and aging processes, as discussed further in Section 3.2.5.

293 Overall, the volatility characteristics across OA factors suggest that oxidation state alone does not fully explain
294 volatility. Rather, volatility is shaped by a combination of emission source, emission timing, temperature, and
295 atmospheric processing. These findings highlight the importance of integrating both chemical and physical
296 characterization to better understand OA formation and aging across seasons.

297 **3.3 Aging effect on volatility from 2D VBS**

298 Generally, the oxygen-to-carbon ($O:C$) ratio of organic aerosols (OA) is inversely related to their volatility. As $O:C$
299 increases, the effective saturation concentration (C^*) typically decreases, resulting in lower volatility (Donahue et
300 al., 2006; Jimenez et al., 2009). This relationship arises because the addition of oxygen-containing functional
301 groups (e.g., hydroxyl, carboxyl, carbonyl) increases molecular weight and enhances intermolecular interactions
302 such as hydrogen bonding, thereby reducing vapor pressure. Moreover, oxidative aging often leads to
303 oligomerization or functionalization, promoting particle-phase retention.

304 However, in this study, the most oxidized OA factor—MO-OOA, with an $O:C$ ratio of 1.15—exhibited
305 unexpectedly high volatility. Its volatility distribution was skewed toward SVOCs and IVOCs (Fig. 5), and its rapid
306 mass loss in MFR thermograms (Fig. S9) further indicated low thermal stability. This observation appears to



307 contradict the expected inverse relationship between O:C and volatility but may be explained by alternative
308 oxidation mechanisms and specific environmental conditions.

309 MO-OOA concentrations increased during haze episodes—characterized by reduced ozone levels, low solar
310 radiation and elevated aerosol mass concentrations (Fig. 6 and Fig. S6, yellow shading). The suppressed ozone
311 likely indicates lower OH radical production via O₃ photolysis, leading to a low-OH oxidation regime. Under such
312 conditions, particle-phase autoxidation involving RO₂ radicals can become the dominant oxidation pathway. These
313 processes tend to produce highly oxidized but relatively low-molecular-weight products (Ehn et al., 2014; Zhao et
314 al., 2023). Unlike classical OH-initiated, multi-generational aging—which increases molecular mass and reduces
315 volatility—fragmentation-dominated oxidation can cleave larger precursors into smaller oxygenated compounds,
316 resulting in higher volatility despite elevated O:C. Furthermore, high aerosol mass loadings during haze events
317 provide abundant surface area for the uptake of semi-volatile species. This facilitates the condensation of even
318 relatively volatile, oxidized compounds onto particles (Fig. 6). The net result is an apparent increase in both
319 oxidation state and volatility of OA, as reported in aging studies under stagnant and polluted conditions (Jimenez
320 et al., 2009; Ng et al., 2016).

321 In line with these reports, our results also revealed a decoupling between O:C and volatility, with MO-OOA
322 showing high volatility despite its elevated O:C ratio (~1.15). While this behavior has been observed in other urban
323 environments, this study provides one of the first detailed thermodynamic assessments of this decoupling under
324 winter haze conditions in Seoul using real-time TD-AMS measurements. Supporting this interpretation, MO-OOA
325 in this study was characterized by a consistently high *f*₄₄ (CO₂⁺) signal and a relatively stable *f*₄₃ (C₂H₃O⁺) signal
326 compared to LO-OOA (Fig. S8b). During specific periods when MO-OOA concentrations increased, only *f*₄₄ was
327 noticeably enhanced, while *f*₄₃ remained flat (Fig. 6). This temporal pattern—elevated *f*₄₄ without corresponding
328 changes in *f*₄₃—is a typical signature of highly oxidized and fragmented organic aerosol and suggests advanced
329 aging dominated by fragmentation rather than functionalization (Kroll et al., 2009). Thus, although MO-OOA had
330 a high O:C ratio, its elevated volatility likely reflects oxidation dominated by autoxidation, fragmentation, and
331 condensation of small oxygenated fragments under conditions of limited OH availability and high particulate
332 surface area.

333 This unexpected volatility behavior of highly oxidized MO-OOA highlights the need for secondary organic aerosol
334 (SOA) models to incorporate fragmentation-dominated oxidation pathways—especially under haze conditions



335 where conventional assumptions linking O:C to volatility may break down. Including such mechanisms could
336 improve model accuracy in representing OA aging and volatility in urban air quality simulations.

337 **4 Conclusions**

338 This study offers a detailed characterization of wintertime submicron aerosols (PM₁) in Seoul by integrating
339 chemical composition, volatility behavior, and source apportionment to better understand their formation and
340 atmospheric evolution. Organic aerosols (OA), particularly secondary organic aerosols (SOA), were the dominant
341 PM₁ component, highlighting the significance of oxidative processes even during cold seasons. A notable result is
342 the successful real-time resolution of a nitrogen-containing organic aerosol (NOA) factor, enabled by cold, humid
343 meteorological conditions that enhanced the partitioning and stabilization of amine-derived compounds. The NOA
344 factor was characterized by tracer ions associated with low-molecular-weight alkylamines such as TMA, DMA,
345 and MA, which likely originated from biomass combustion.

346

347 Volatility analysis revealed distinct thermodynamic behavior across OA sources. Primary OA factors such as HOA,
348 BBOA, and COA exhibited relatively high volatility, while LO-OOA showed low volatility and a higher oxidation
349 state, consistent with aged, low-volatility material. The similarity in volatility distributions and diurnal patterns
350 between BBOA and NOA suggests that biomass combustion under wintertime conditions is a likely contributor to
351 both primary organic and nitrogenous aerosol formation.

352

353 Interestingly, MO-OOA—despite its high oxygen-to-carbon (O:C) ratio—exhibited elevated volatility, diverging
354 from the expected inverse relationship between oxidation state and volatility. This suggests that under stagnant,
355 polluted conditions with suppressed ozone and OH radical levels, particle-phase autooxidation and fragmentation
356 pathways may dominate over traditional OH-initiated aging, yielding highly oxidized yet semi-volatile products.
357 These findings highlight the importance of coupling high-resolution chemical and physical aerosol measurements
358 to better understand OA formation processes and properties within urban air quality frameworks. Consequently,
359 air quality models should incorporate diverse oxidation mechanisms and avoid assuming a direct link between
360 oxidation state and volatility.



361 **Acknowledgements**

362 This work was supported by the National Research Foundation of Korea (NRF) grant funded by the Korea government (MSIT)
363 (RS-2025-00514570), the project “development of SMaRT based aerosol measurement and analysis systems for the evaluation
364 of climate change and health risk assessment” operated by Seoul National University (900-20240101).

365 **Author Contributions**

366 Hwajin Kim designed and prepared the manuscript. Jiwoo Jeong operated the TD-AMS and analyse the data. Jihye Moon
367 analyse the data. Hyungu Kang analyse the volatility of OA.

368 **Conflicts of Interest**

369 Authors declare that they have no conflict of interest.

370

371

372

373

374

375

376

377

378

379

380

381

382

383

384

385

386

387

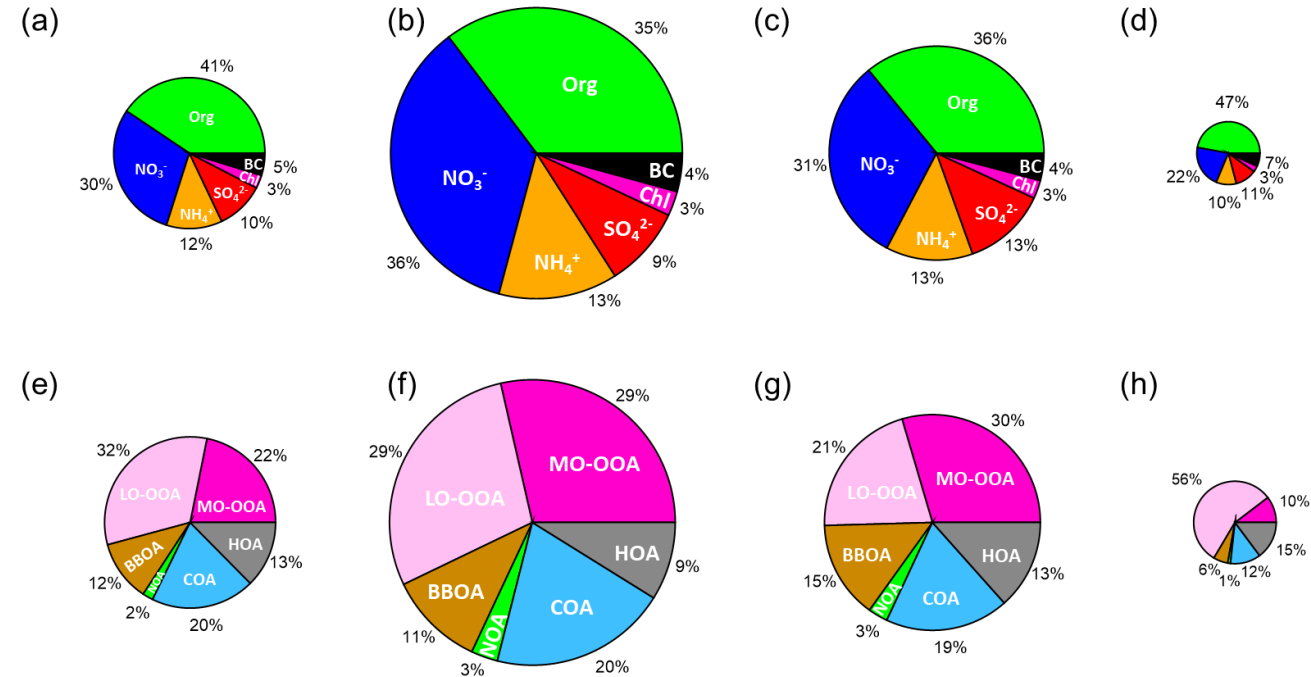
388

389

390



Tables and Figures



	Period	Standard	Avg. Mass conc.($\mu\text{g m}^{-3}$)
Total	2019.11.28 ~ 2019.12.28		Avg PM ₁ = 26.37
Clean	2019.12.04 ~ 2019.12.06	Daily PM ₁ < 10.00 $\mu\text{g m}^{-3}$	Avg PM ₁ = 9.98
Haze 1	2019.12.07 ~ 2019.12.11	Daily PM ₁ > 30.00 $\mu\text{g m}^{-3}$	Avg PM ₁ = 51.88
Haze 2	2019.12.21 ~ 2019.12.25	Daily PM ₁ > 30.00 $\mu\text{g m}^{-3}$	Avg PM ₁ = 37.71

Figure 1. Compositional pie charts of PM₁ species for (a) the entire study period, (b) haze period 1, (c) haze period 2, and (d) a clean period; and of each OA source for (e) the entire study period, (f) haze period 1, (g) haze period 2, and (h) the clean period. Table. Standard and average PM₁ mass concentrations during the entire study period, haze period 1, haze period 2, and the clean period.

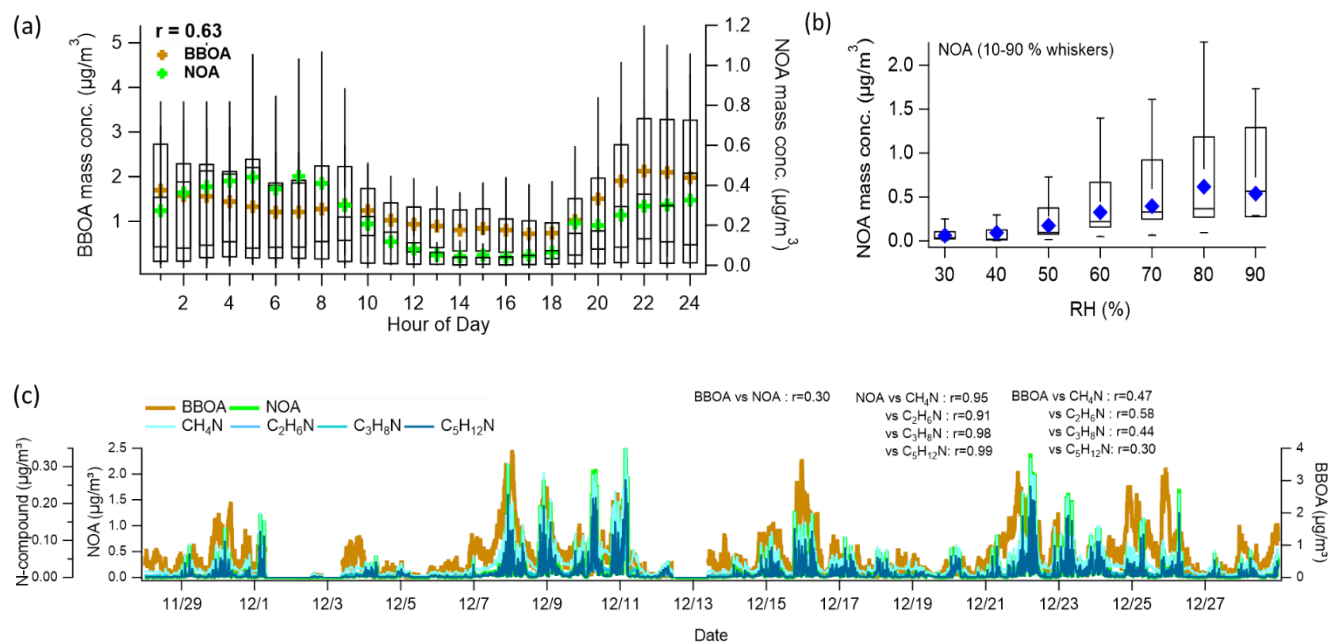


Figure 2. (a) Diurnal mean profiles of NOA and BBOA. Whiskers denote the 90th and 10th percentiles; box edges represent the 75th and 25th percentiles; the horizontal line indicates the median, and the colored marker shows the mean. The diurnal correlation between NOA and BBOA mean values is 0.63. (b) Relative humidity (RH)-binned nighttime (19:00–05:00) profile of NOA. Box and whisker definitions are the same as in panel (a). (c) Time series of NOA, BBOA, and amine-related ions (CH_4N^+ , $\text{C}_2\text{H}_6\text{N}^+$, $\text{C}_3\text{H}_8\text{N}^+$, $\text{C}_5\text{H}_{12}\text{N}^+$), along with their correlations with NOA and BBOA.

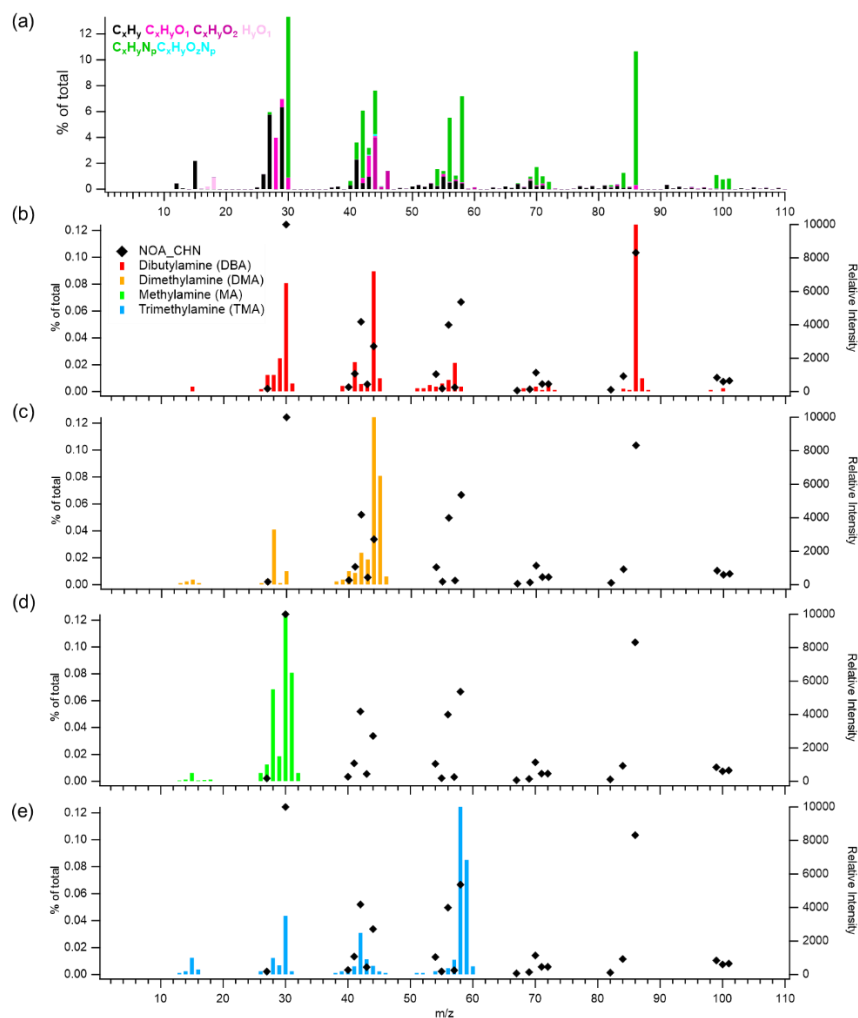
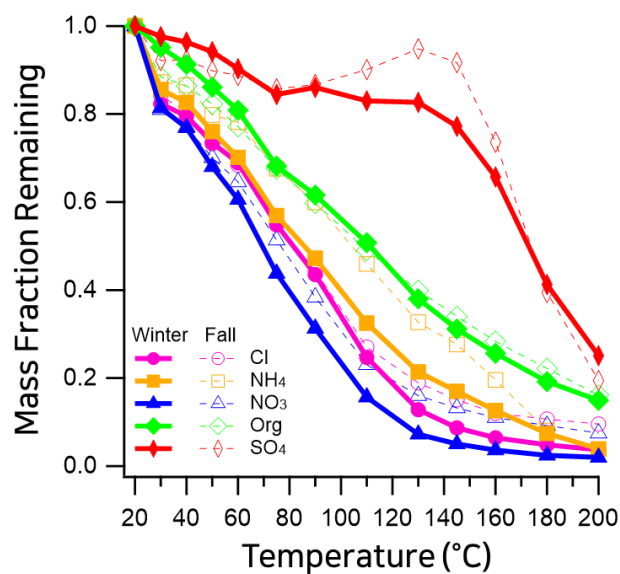


Figure 3. Mass spectra of (a) the NOA factor resolved by PMF analysis in this study, and reference spectra of amines from the NIST library: (b) dibutylamine (DBA), (c) dimethylamine (DMA), (d) methylamine (MA), and (e) trimethylamine (TMA). In panels (b)–(e), the left y-axis indicates the contribution of CHN-containing ions in the NOA factor (% of total), while the right y-axis shows the relative intensity of each compound’s mass spectrum from the NIST library.



429 **Figure 4.** Mass fraction remaining (MFR) of non-refractory (NR) aerosol species measured in Seoul during fall (solid lines)
 430 and winter (dashed lines) 2019 using a thermodenuder coupled to a high-resolution time-of-flight aerosol mass spectrometer
 431 (HR-ToF-AMS). Species include organics (magenta), nitrate (blue), sulfate (orange), ammonium (green), and chloride (red).

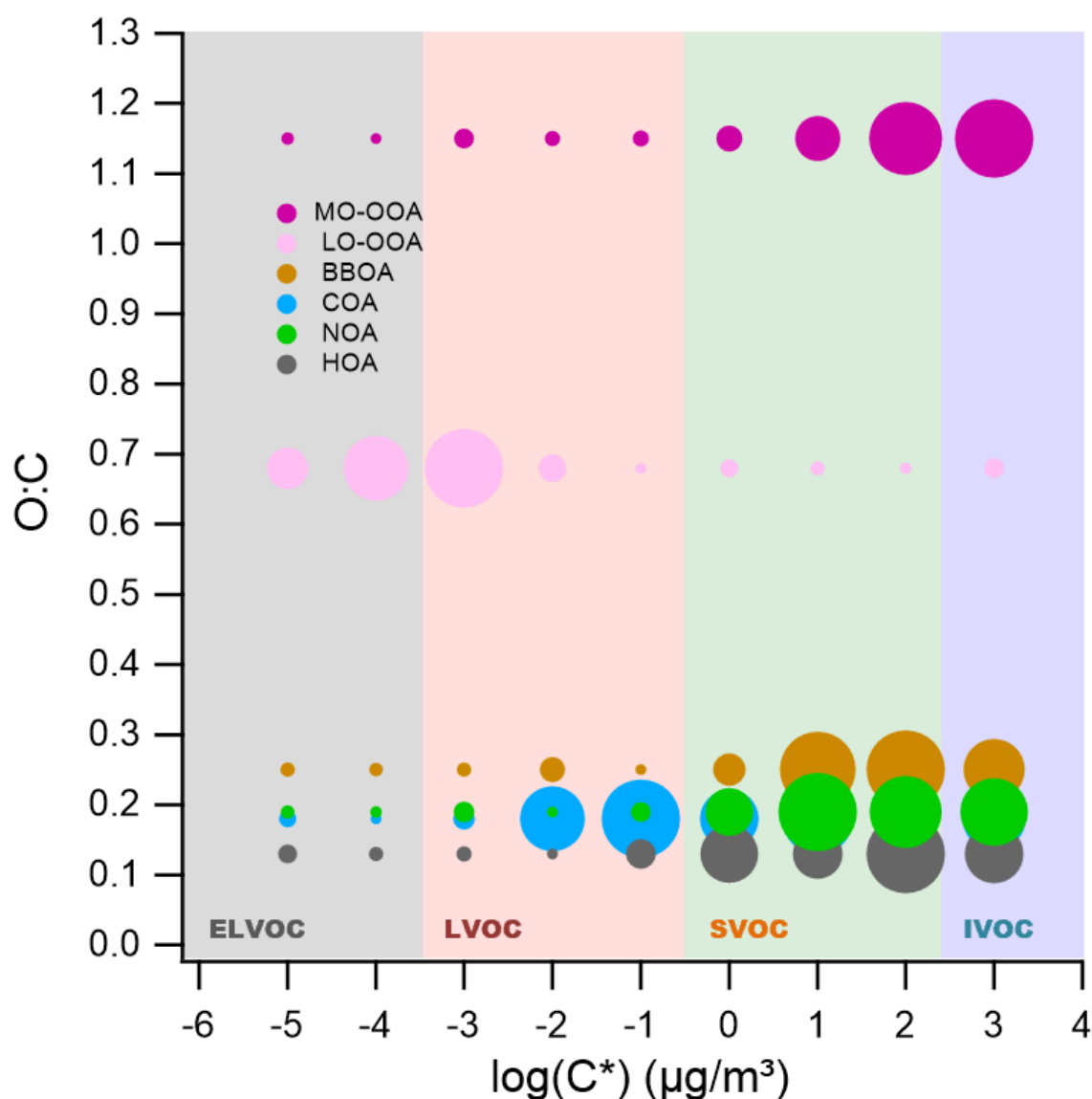


Figure 5. Two-dimensional volatility basis set (2D-VBS) representation of organic aerosol (OA) sources identified in winter 2019 in Seoul. The plot illustrates the relationship between the oxygen-to-carbon (O:C) ratio and the effective saturation concentration (C^*) for each OA source resolved via positive matrix factorization (PMF). Solid circles represent the volatility distribution across C^* bins, with marker size proportional to the mass fraction within each bin for the given source. Shaded regions correspond to different volatility classes: extremely low-volatility organic compounds (ELVOCs), low-volatility organic compounds (LVOCs), semi-volatile organic compounds (SVOCs), and intermediate-volatility organic compounds (IVOCs), delineated by their C^* values.

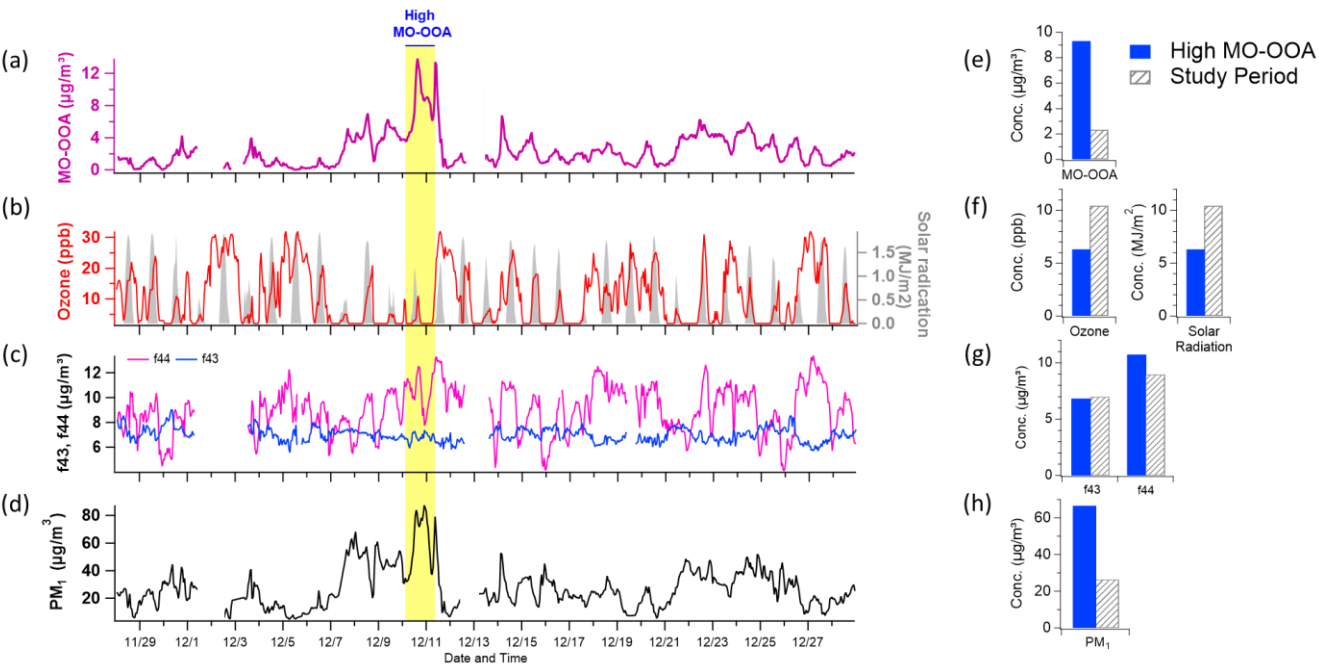


Figure 6. Time series plots of (a) MO-OOA concentration, (b) ozone (O_3) and solar radiation, (c) f_{44} and f_{43} (indicative of oxidation state), and (d) total PM_{10} concentration. The period characterized by elevated MO-OOA levels is highlighted in bright yellow. Panels (e)–(h) present comparative distributions of these variables—MO-OOA, O_3 and solar radiation, f_{44} and f_{43} , and PM_{10} —between the high MO-OOA period (shaded in blue) and the entire measurement period (indicated by gray hatching).



471
 472
 473
 474
 475
 476
 477
 478
 479
 480

481 **References**

- 482 Ghim, Y. S., Moon, K.-C., Lee, S., Kim, Y. P., 2005. Visibility trends in Korea during the past two decades. *J. Air Waste*
 483 *Manag. Assoc.* 55, 73–82. <https://doi.org/10.1080/10473289.2005.10464599>
- 484 Zhao, H., Che, H., Zhang, X., Ma, Y., Wang, Y., Wang, H., Wang, Y., 2013. Characteristics of visibility and particulate matter
 485 (PM) in an urban area of Northeast China. *Atmos. Pollut. Res.* 4, 427–434. <https://doi.org/10.5094/APR.2013.049>
- 486 Hamanaka, R. B., Mutlu, G. M., 2018. Particulate matter air pollution: Effects on the cardiovascular system. *Front. Endocrinol.*
 487 9, 680. <https://doi.org/10.3389/fendo.2018.00680>
- 488 Manisalidis, I., Stavropoulou, E., Starvropoulos, A., Bezirtzoglou, E., 2020. Environmental and health impacts of air pollution:
 489 a review. *Front. Public Health* 8, 14. <https://doi.org/10.3389/fpubh.2020.00014>
- 490 IPCC, 2021. *Climate Change 2021: The Physical Science Basis*. Contribution of Working Group I to the Sixth Assessment
 491 Report of the Intergovernmental Panel on Climate Change, edited by Masson-Delmotte, V., Zhai, P., Pirani, A., Connors,
 492 S.L., Péan, C., Berger, S., et al. Cambridge University Press, Cambridge, UK and New York, NY, USA, pp. 817–922.
 493 <https://doi.org/10.1017/9781009157896.008>
- 494 Zhang, Q., Jimenez, J. L., Canagaratna, M. R., Allan, J. D., Coe, H., Ulbrich, I., Alfarra, M. R., Takami, A., Middlebrook, A.
 495 M., Sun, Y. L., Dzepina, K., Dunlea, E., Docherty, K., DeCarlo, P., Salcedo, D., Onasch, T. B., Jayne, J. T., Miyoshi, T.,
 496 Shimono, A., Hatakeyama, N., Takegawa, N., Kondo, Y., Schneider, J., Drewnick, F., Weimer, S., Demerjian, K. L.,
 497 Williams, P. I., Bower, K. N., Bahreini, R., Cottrell, L., Griffin, R. J., Rautianen, J., Worsnop, D. R., 2007. Ubiquity and
 498 dominance of oxygenated species in organic aerosols in anthropogenically-influenced Northern Hemisphere mid-latitudes.
 499 *Geophys. Res. Lett.* 34, L13801. <https://doi.org/10.1029/2007GL029979>
- 500 Jimenez, J. L., Canagaratna, M. R., Donahue, N. M., Prevot, A. S. H., Zhang, Q., Kroll, J. H., ... Worsnop, D. R., 2009.
 501 Evolution of organic aerosols in the atmosphere. *Science* 326, 1525–1529. <https://doi.org/10.1126/science.1180353>



- 502 Hallquist, M., Wenger, J. C., Baltensperger, U., Rudich, Y., Simpson, D., Claeys, M., ... Seinfeld, J. H., 2009. The formation,
503 properties and impact of secondary organic aerosol: current and emerging issues. *Atmos. Chem. Phys.* 9, 5155–5236.
504 <https://doi.org/10.5194/acp-9-5155-2009>
- 505 Robinson, A. L., Donahue, N. M., Shrivastava, M. K., Weitkamp, E. A., Sage, A. M., Grieshop, A. P., Lane, T. E., Pierce, J.
506 R., Pandis, S. N., 2007. Rethinking organic aerosols: Semivolatile emissions and photochemical aging. *Science* 315, 1259–
507 1262. <https://doi.org/10.1126/science.1133061>
- 508 Donahue, N. M., Robinson, A. L., Stanier, C. O., Pandis, S. N., 2006. Coupled partitioning, dilution, and chemical aging of
509 semivolatile organics. *Environ. Sci. Technol.* 40, 2635–2643. <https://doi.org/10.1021/es052297c>
- 510 Ng, N. L., Canagaratna, M. R., Zhang, Q., Jimenez, J. L., Tian, J., Ulbrich, I. M., Kroll, J. H., Docherty, K. S., Chhabra, P. S.,
511 Bahreini, R., Murphy, S. M., Seinfeld, J. H., Hildebrandt, L., Donahue, N. M., DeCarlo, P. F., Lanz, V. A., Prévôt, A. S.
512 H., Dinar, E., Rudich, Y., Worsnop, D. R., 2010. Organic aerosol components observed in Northern Hemispheric datasets
513 from Aerosol Mass Spectrometry. *Atmos. Chem. Phys.* 10, 4625–4641. <https://doi.org/10.5194/acp-10-4625-2010>
- 514 Cappa, C. D., Jimenez, J. L., 2010. Quantitative estimates of the volatility of ambient organic aerosol. *Atmos. Chem. Phys.*
515 10, 5409–5424. <https://doi.org/10.5194/acp-10-5409-2010>
- 516 Sinha, A., George, I., Holder, A., Preston, W., Hays, M., Grieshop, A. P., 2023. Development of volatility distributions for
517 organic matter in biomass burning emissions. *Environ. Sci. Adv.* 3, 11–23. <https://doi.org/10.1039/D2EA00080F>
- 518 Glasius, M., Goldstein, A. H., 2016. Recent discoveries and future challenges in atmospheric organic chemistry. *Environ. Sci.*
519 *Technol.* 50, 2754–2764. <https://doi.org/10.1021/acs.est.5b05105>
- 520 Matsui, H., Koike, M., Takegawa, N., Kondo, Y., Griffin, R. J., Miyazaki, Y., Yokouchi, Y., Ohara, T., 2009. Secondary
521 organic aerosol formation in urban air: Temporal variations and possible contributions from unidentified hydrocarbons. *J.*
522 *Geophys. Res. Atmos.* 114, D02209. <https://doi.org/10.1029/2008JD010164>
- 523 Jiang, F., Liu, Q., Huang, X., Wang, T., Zhuang, B., Xie, M., 2012. Regional modelling of secondary organic aerosol over
524 China using WRF/Chem. *J. Aerosol Sci.* 53, 50–61. <https://doi.org/10.1016/j.jaerosci.2011.09.003>
- 525 Li, J., Zhang, M., Wu, F., Sun, Y., Tang, G., 2017. Assessment of the impacts of aromatic VOC emissions and yields of SOA
526 on SOA concentrations with the air quality model RAMS-CMAQ. *Atmos. Environ.* 158, 105–115.
527 <https://doi.org/10.1016/j.atmosenv.2017.03.035>
- 528 Zhao, B., Wang, S., Donahue, N. M., Jathar, S. H., Huang, X., Wu, W., ... & Hao, J. (2016). Quantifying the effect of organic
529 aerosol aging and intermediate-volatility emissions on regional-scale aerosol pollution in China. *Scientific Reports*, 6,
530 28815. <https://doi.org/10.1038/srep28815>
- 531 Kang, H. G., Kim, Y., Collier, S., Zhang, Q., Kim, H., 2022. Volatility of springtime ambient organic aerosol derived with
532 thermodenuder aerosol mass spectrometry in Seoul, Korea. *Environ. Pollut.* 310, 119203.
533 <https://doi.org/10.1016/j.envpol.2022.119203>
- 534 Huang, X.-F., He, L.-Y., Hu, M., Canagaratna, M. R., Sun, Y., Zhang, Q., Worsnop, D. R., 2010. Highly time-resolved
535 chemical characterization of atmospheric submicron particles during 2008 Beijing Olympic Games using an Aerodyne



- 536 High-Resolution Aerosol Mass Spectrometer. *Atmos. Chem. Phys.* 10, 8933–8945. <https://doi.org/10.5194/acp-10-8933->
537 2010
- 538 Mohr, C., DeCarlo, P. F., Heringa, M. F., Chirico, R., Slowik, J. G., Richter, R., Reche, C., Alastuey, A., Querol, X., Seco, R.,
539 Peñuelas, J., Jiménez, J. L., Crippa, M., Zimmermann, R., Baltensperger, U., Prévôt, A. S. H., 2012. Identification and
540 quantification of organic aerosol from cooking and other sources in Barcelona using aerosol mass spectrometer data.
541 *Atmos. Chem. Phys.* 12, 1649–1665. <https://doi.org/10.5194/acp-12-1649-2012>
- 542 Xu, L., Kollman, M. S., Song, C., Shilling, J. E., Ng, N. L., 2014. Effects of NO_x on the volatility of secondary organic aerosol
543 from isoprene photooxidation. *Environ. Sci. Technol.* 48, 2253–2262. <https://doi.org/10.1021/es404842g>
- 544 Grieshop, A. P., Logue, J. M., Donahue, N. M., Robinson, A. L., 2009. Laboratory investigation of photochemical oxidation
545 of organic aerosol from wood fires 1: Measurement and simulation of organic aerosol evolution. *Atmos. Chem. Phys.* 9,
546 1263–1277. <https://doi.org/10.5194/acp-9-1263-2009>
- 547 Kim, H., Zhang, Q., Bae, G.-N., Kim, J.Y., Lee, S.B., 2017. Sources and atmospheric processing of winter aerosols in Seoul,
548 Korea: Insights from real-time measurements using a high-resolution aerosol mass spectrometer. *Atmos. Chem. Phys.* 17,
549 2009–2033. <https://doi.org/10.5194/acp-17-2009-2017>
- 550 DeCarlo, P. F., Kimmel, J. R., Trimborn, A., Northway, M. J., Jayne, A. E., Aiken, A. C., ... & Jimenez, J. L. (2006). Field-
551 deployable, high-resolution, time-of-flight aerosol mass spectrometer. *Analytical Chemistry*, 78(24), 8281–8289.
552 <https://doi.org/10.1021/ac061249>
- 553 Canagaratna, M. R., Jimenez, J. L., Kroll, J. H., Chen, Q., Kessler, S. H., Massoli, P., ... & Worsnop, D. R. (2015). Elemental
554 ratio measurements of organic compounds using aerosol mass spectrometry: Improved sensitivity and intercomparability.
555 *Atmospheric Chemistry and Physics*, 15(1), 253–272. <https://doi.org/10.5194/acp-15-253-2015>
- 556 Paatero, P., Tapper, U., 1994. Positive matrix factorization – A nonnegative factor model with optimal utilization of error
557 estimates of data values. *Environmetrics* 5, 111–126. <https://doi.org/10.1002/env.3170050203>
- 558 Ulbrich, I. M., Canagaratna, M. R., Zhang, Q., Worsnop, D. R., Jimenez, J. L., 2009. Interpretation of organic components
559 from Positive Matrix Factorization of aerosol mass spectrometric data. *Atmos. Chem. Phys.* 9, 2891–2918.
560 <https://doi.org/10.5194/acp-9-2891-2009>
- 561 Zhang, Q., Jimenez, J. L., Canagaratna, M. R., Ulbrich, I. M., Ng, N. L., Worsnop, D. R., Sun, Y., 2011. Understanding
562 atmospheric organic aerosols via factor analysis of aerosol mass spectrometry: A review. *Anal. Bioanal. Chem.* 401, 3045–
563 3067. <https://doi.org/10.1007/s00216-011-5355-y>
- 564 Huffman, J. A., Docherty, K. S., Aiken, A. C., Cubison, M. J., Ulbrich, I. M., DeCarlo, P. F., Jimenez, J. L., 2009. Chemically-
565 resolved aerosol volatility measurements from two megacity field studies. *Atmos. Chem. Phys.* 9, 7161–7182.
566 <https://doi.org/10.5194/acp-9-7161-2009>
- 567 Saha, P. K., Khlystov, A., Grieshop, A. P., 2014. Determining aerosol volatility parameters using a “dual thermodenuder”
568 system: Application to laboratory-generated organic aerosols. *Aerosol Sci. Technol.* 49, 620–632.
569 <https://doi.org/10.1080/02786826.2015.1056769>



- 570 Zhou, S., Collier, S., Jaffe, D. A., Briggs, N. L., Hee, J., Sedlacek III, A. J., Kleinman, L., & Lewis, K., 2017. Regional
571 influence of wildfires on aerosol chemistry in the western US and insights into atmospheric aging of biomass burning
572 organic aerosol. *Atmospheric Chemistry and Physics*, 17, 2477–2493. <https://doi.org/10.5194/acp-17-2477-2017>
- 573 Riipinen, I., Pierce, J. R., Donahue, N. M., Pandis, S. N., 2010. Equilibration time scales of organic aerosol inside
574 thermodenuders: Kinetics versus equilibrium thermodynamics. *Atmos. Environ.* 44, 597–607.
575 <https://doi.org/10.1016/j.atmosenv.2009.11.022>
- 576 Karnezi, E., Riipinen, I., Pandis, S. N., 2014. Measuring the atmospheric organic aerosol volatility distribution: a theoretical
577 analysis. *Atmos. Meas. Tech.* 7, 2953–2965. <https://doi.org/10.5194/amt-7-2953-2014>
- 578 Chen, Y., Wang, Z., Wang, Y., Zheng, X., Fu, P., Kawamura, K., Zhang, Y., 2021. Characterization of nitrogen-containing
579 organic aerosol in Guangzhou, China: seasonal variation, formation mechanism and source apportionment. *Atmos. Chem.*
580 *Phys.* 21, 4329–4344. <https://doi.org/10.5194/acp-21-4329-2021>
- 581 Hayes, P. L., Ortega, A. M., Cubison, M. J., Froyd, K. D., Zhao, Y., Cliff, S. S., ... Jimenez, J. L., 2013. Organic aerosol
582 composition and sources in Pasadena, California, during the 2010 CalNex campaign. *J. Geophys. Res. Atmos.* 118, 9233–
583 9257. <https://doi.org/10.1002/jgrd.50530>
- 584 Sun, Y., Jiang, Q., Wang, Z., Fu, P., Li, J., Yang, T., Yin, Y., 2011. Investigation of the sources and evolution processes of
585 severe haze pollution in Beijing in January 2013. *J. Geophys. Res. Atmos.* 119, 4380–4398.
586 <https://doi.org/10.1002/2014JD021641>
- 587 Baek, K. M., Park, E. H., Kang, H., Ji, M. J., Park, H. M., & Kim, Y. P., 2022. Seasonal characteristics of atmospheric water-
588 soluble organic nitrogen in PM_{2.5} in Seoul, Korea: Source and atmospheric processes of free amino acids and aliphatic
589 amines. *Science of the Total Environment*, 807, 150785. <https://doi.org/10.1016/j.scitotenv.2021.150785>
- 590 Milic, A., Hopke, P. K., McWhinney, R. D., Thomson, E. M., Healy, R. M., 2016. Impact of relative humidity on amine and
591 aminium salt aerosol formation from atmospheric reactions. *Atmos. Chem. Phys.* 16, 14527–14543.
592 <https://doi.org/10.5194/acp-16-14527-2016>
- 593 Ge, X., Wexler, A. S., Clegg, S. L., 2011. Atmospheric amines – Part I. A review. *Atmos. Environ.* 45, 524–546.
594 <https://doi.org/10.1016/j.atmosenv.2010.10.012>
- 595 Poste, A. E., Grung, M., & Wright, R. F. 2014. Amines and amine-related compounds in surface waters: A review of sources,
596 concentrations and aquatic toxicity. *Science of the Total Environment*, 487, 122–135.
597 <https://doi.org/10.1016/j.scitotenv.2014.03.113>
- 598 He, J., Liu, H., Shan, P., Zhang, K., Qin, Y., & Liu, L. 2016. Supported-gas-membrane process for removal and recovery of
599 aliphatic amines from aqueous streams. *Chemical Engineering Science*, 144, 110–119.
600 <https://doi.org/10.1016/j.ces.2016.01.018>
- 601 You, Y., Renbaum-Wolff, L., Carreras-Sospedra, M., Dabdub, D., Bertram, A. K., Martin, S. T., et al., 2014. Images reveal
602 that amines promote the heterogeneous reaction of epoxides in model organic aerosols. *J. Phys. Chem. Lett.* 5, 3211–
603 3215. <https://doi.org/10.1021/jz501268k>



- 604 Yao, L., Wang, M. Y., Wang, X. K., Zhang, W. Q., Liu, Y., Li, L., et al., 2016. Atmospheric new particle formation from
605 sulfuric acid and amines in a Chinese megacity. *Sci. Bull.* 61, 939–945. <https://doi.org/10.1007/s11434-016-1083-0>
- 606 Kim, H., Zhang, Q., Sun, Y., Bae, G. N., Lee, B. E., Park, K., ... & Kim, Y. J. 2020. Measurement report: Characterization of
607 severe spring haze episodes and influences of long-range transport in the Seoul metropolitan area in March 2019.
608 *Atmospheric Chemistry and Physics*, 20(18), 11527–11545. <https://doi.org/10.5194/acp-20-11527-2020>
- 609 Jeon, J., Chen, Y., Kim, H., 2023. Influence of meteorology on emission sources and physicochemical properties of particulate
610 matter in Seoul, Korea during heating period. *Atmos. Environ.* 301, 119733.
611 <https://doi.org/10.1016/j.atmosenv.2023.119733>
- 612 Zhang, Q., Alfara, M. R., Worsnop, D. R., Allan, J. D., Coe, H., Canagaratna, M. R., ... & Jimenez, J. L. 2005. Deconvolution
613 and quantification of hydrocarbon-like and oxygenated organic aerosols based on aerosol mass spectrometry.
614 *Environmental Science & Technology*, 39(13), 4938–4952. <https://doi.org/10.1021/es048568l>
- 615 Simoneit, B. R. T. 2002. Biomass burning – a review of organic tracers for smoke from incomplete combustion. *Applied*
616 *Geochemistry*, 17(3), 129–162. [https://doi.org/10.1016/S0883-2927\(01\)00061-0](https://doi.org/10.1016/S0883-2927(01)00061-0)
- 617 Cubison, M. J., Ortega, A. M., Hayes, P. L., Farmer, D. K., Day, D., Lechner, M. J., ... & Jimenez, J. L. 2011. Effects of aging
618 on organic aerosol from open biomass burning smoke in aircraft and laboratory studies. *Atmospheric Chemistry and*
619 *Physics*, 11(23), 12049–12064. <https://doi.org/10.5194/acp-11-12049-2011>
- 620 Xu, L., Williams, L. R., Young, D. E., Allan, J. D., Coe, H., Massoli, P., Fortner, E., Chhabra, P., Herndon, S., Brooks, W. A.,
621 Jayne, J. T., Worsnop, D. R., Aiken, A. C., Liu, S., Gorkowski, K., Dubey, M. K., Fleming, Z. L., Visser, S., Prévôt, A.
622 S. H., Ng, N. L., 2016. Wintertime aerosol chemical composition, volatility, and spatial variability in the Greater London
623 Area. *Atmos. Chem. Phys.* 16, 1139–1160. <https://doi.org/10.5194/acp-16-1139-2016>
- 624 Feng, T., Wang, Y., Hu, W., Zhu, M., Song, W., Chen, W., ... Wang, X., 2023. Impact of aging on the sources, volatility, and
625 viscosity of organic aerosols in Chinese outflows. *Atmos. Chem. Phys.* 23, 611–636. [https://doi.org/10.5194/acp-23-611-](https://doi.org/10.5194/acp-23-611-2023)
626 2023
- 627 Scott, W. D., & Cattell, F. C. R. 1979. Vapor pressure of ammonium sulfates. *Atmospheric Environment* (1967), 13(6), 987–
628 1000. [https://doi.org/10.1016/0004-6981\(79\)90174-4](https://doi.org/10.1016/0004-6981(79)90174-4)
- 629 Donahue, N. M., Robinson, A. L., Pandis, S. N., 2009. Atmospheric organic particulate matter: From smoke to secondary
630 organic aerosol. *Atmos. Environ.* 43, 94–106. <https://doi.org/10.1016/j.atmosenv.2008.09.055>
- 631 Ehn, M., Thornton, J. A., Kleist, E., Sipilä, M., Junninen, H., Pullinen, I., ... & Kulmala, M. 2014. A large source of low-
632 volatility secondary organic aerosol. *Nature*, 506(7489), 476–479. <https://doi.org/10.1038/nature13032>
- 633 Kroll, J. H., Smith, J. D., Che, D. L., Kessler, S. H., Worsnop, D. R., Wilson, K. R., 2009. Measurement of fragmentation and
634 functionalization pathways in the heterogeneous oxidation of oxidation organic aerosol. *Environ. Sci. Technol.* 43, 7826–
635 7833. <https://doi.org/10.1021/es901683r>



636 Xu, L., Williams, L.R., Young, D.E., Allan, J.D., Coe, H., Massoli, P., Fortner, E., Chhabra, P., Herndon, S., Brooks, W.A.,
637 et al., 2016. Wintertime aerosol chemical composition, volatility, and spatial variability in the greater London area. *Atmos.*
638 *Chem. Phys.* 16, 1139–1160. <https://doi.org/10.5194/acp-16-1139-2016>
639 Cao, L.-M., Huang, X.-F., Li, Y.-Y., Hu, M., He, L.-Y., 2018. Volatility measurement of atmospheric submicron aerosols in
640 an urban atmosphere in southern China. *Atmos. Chem. Phys.* 18, 1729–1743. <https://doi.org/10.5194/acp-18-1729-2018>
641 Xu, W., Xie, C., Karnezi, E., Zhang, Q., Wang, J., Pandis, S.N., Ge, X., Zhang, J., An, J., Wang, Q., et al., 2019. Summertime
642 aerosol volatility measurements in Beijing, China. *Atmos. Chem. Phys.* 19, 10205–10216. [https://doi.org/10.5194/acp-](https://doi.org/10.5194/acp-19-10205-2019)
643 19-10205-2019
644